tions (Fig. 4). The layer thicknesses observed (a = 0.90 μm for the 400-μm fibers; a = 0.45 μm for the 200-μm fibers) correspond well to the measured reflectivity spectra. The fibers have a hole in the center, because of the choice of a hollow rod as the preform substrate, which experienced some nonuniform deformation during draw. The rolled-up mirror structure included a double outer layer of PES for mechanical protection, creating a noticeable absorption peak in the reflectivity spectrum at ~3.2 μm (Fig. 3A).

A combination of spectral and direct imaging data demonstrates excellent agreement with the photonic band diagram. Table 1 summarizes this agreement for the 400-μm-OD fibers by comparing the calculated photonic band gap locations shown in Fig. 1, together with the SEM-measured period spacing of a = 0.90 μm, to the empirical spectral reflection data shown in Fig. 3A. The measured gap width (range to midrange ratio) of the fundamental gap for the 400-μm-OD fiber is 27%, compared to 29% in the photonic band diagram.

In light of these results, we can evaluate the relative importance of various physical properties in creating these drawn omnidirectional dielectric mirror fibers. The matching of rheological behavior in elongation at the draw temperature is the key factor in our fiber production. At the draw temperature, the materials should be fluid enough to elongate without sizable stress buildup, yet not so fluid that the mirror layers lose their periodicity. Coefficient of thermal expansion (CTE) may also play an important role in the adhesion and integrity of thin films during any thermal quenching procedure. PES has a linear CTE of 55 × 10^{-6}/°C (*23*), whereas As_2Se_3 has a linear CTE of 25 ×10^{-6}/°C (*22*). In the mirror fiber geometry described here, this CTE mismatch could act to strengthen the outer As_2Se_3 layers by placing them in compression as the PES core of the fiber cools and contracts well below the glass transition of As_2Se_3. This materials combination facilitated the thermal fabrication of high-performance dielectric mirrors in a conformal, flexible fiber geometry.

References and Notes

1. P. Yeh, A. Yariv, E. Marom, *J. Opt. Soc. Am.* **68**, 1196 (1978).
2. J. W. Dai, J. A. Harrington, *Appl. Opt.* **36**, 5072 (1997).
3. Y. Fink *et al.*, *J. Lightwave Technol.* **17**, 2039 (1999).
4. We are also pursuing the application of the types of materials and methods described here to the fabrication of hollow fibers having multiple dielectric layers surrounding a hollow core for the purpose of light guidance.
5. Y. Fink *et al.*, *Science* **282**, 1679 (1998).
6. J. N. Winn, Y. Fink, S. Fan, J. D. Joannopoulos, *Opt. Lett.* **23**, 1573 (1998).
7. P. Yeh, A. Yariv, C. Hong, *J. Opt. Soc. Am.* **67**, 423 (1977).
8. B. Temelkuran, E. L. Thomas, J. D. Joannopoulos, Y. Fink, *Opt. Lett.* **26**, 1370 (2001).
9. H. F. Mahlein, *J. Opt. Soc. Am.* **64**, 647 (1974).
10. P. Baumeister, *Opt. Acta* **8**, 105 (1961).
11. M. F. Weber, C. A. Stover, L. R. Gilbert, T. J. Nevitt, A. J. Ouderkirk, *Science* **287**, 2451 (2000).
12. R. F. Cregan *et al.*, *Science* **285**, 1537 (1999).
13. J. D. Joannopoulos, R. Meade, J. N. Winn, *Photonic Crystals: Molding the Flow of Light* (Princeton Univ. Press, Princeton, NJ, 1995).
14. A. K. Varshneya, *Fundamentals of Inorganic Glasses* (Academic Press, San Diego, CA, 1994).
15. D. W. Van Krevelen, *Properties of Polymers* (Elsevier Scientific, New York, ed. 3, 1990).
16. A. Kucuk, A. G. Clare, L. Jones, *Glass Technol.* **40**, 149 (1999).
17. Z. U. Borisova, *Glassy Semiconductors* (Plenum, New York, 1981).
18. A. K. Varshneya, *J. Non-Cryst. Solids* **273**, 1 (2000).
19. A. B. Seddon, *J. Non-Cryst. Solids* **184**, 44 (1995).
20. W. A. King, A. G. Clare, W. C. LaCourse, *J. Non-Cryst. Solids* **181**, 231 (1995).
21. A. R. Hilton, *J. Non-Cryst. Solids* **2**, 28 (1970).
22. M. Bass, Ed., *Handbook of Optics* (McGraw-Hill, New York, 1995).
23. J. E. Mark, Ed., *Polymer Data Handbook* (Oxford Univ. Press, New York, 1999).
24. C. Sarantos, unpublished data.
25. PES films were purchased from the Goodfellow Corporation, and As_2Se_3 (99.999% pure, metals basis) was purchased from Alfa Aesar/Strem Chemicals. A 2-cm-OD PES rod was made from a PES film of 50 ± 5 μm that was rolled by hand onto a 7-mm hollow borosilicate glass tube and consolidated through heat treatment at 261° to 263°C under vacuum for ~25 min. As_2Se_3 films were deposited by thermal evaporation with a vacuum evaporator (Ladd Industries) on a separate PES film. In situ layer thickness monitoring was carried out with a crystal thickness monitor (Sycon STM100) that was calibrated with a surface profilometer (Tencor P10). An As_2Se_3 film of 6.5 ± 0.4 μm was evaporated at a rate of ~10 nm/s on each side of a thin PES film of 25 ± 2 μm. This As_2Se_3-coated film was then rolled onto the outside of the previously fabricated PES tube and consolidated with a similar vacuum thermal treatment. The hollow Pyrex tube at the core of the PES/As_2Se_3 structure was then etched out with hydrofluoric acid.
26. The preform was lowered at a controlled rate into a three-zone vertical tube furnace (Thermcraft) and pulled from below at controlled speeds with a motorized capstan (Heathway). Fiber diameters were monitored with laser diameter monitors (Beta LaserMike). Fibers were drawn at a central-zone maximum temperature of 295°C at speeds ranging from approximately 1 to 10 m/min, depending on target fiber diameter. The upper zone of the furnace was heated to 240°C, and the lower zone was unheated, but drifted to a temperature of ~150°C.
27. The applicability of the indicated angular range of detection was corroborated by personal communication with M. Friedman of SpectraTech.
28. J. A. Kong, *Electromagnetic Wave Theory* (EMW Publishing, Cambridge, MA, 2000), pp. 370–406.

29. We thank H. Burch for guidance and inspiration; C. H. Sarantos, K. R. Maskaly, E. P. Chan, and M. Frongillo for valuable assistance; and J. Harrington, A. R. Hilton, and E. L. Thomas for support and direction. We also thank K. Hersey, B. Smith, and the MIT Research Laboratory of Electronics for their support. G.R.M. thanks the Fannie and John Hertz Foundation for its support. This work was supported under the following awards: Army Research Office/Defense Advanced Research Projects Agency award DAAD19-01-1-0647; NSF award ECS 0123460; and U.S. Department of Energy award DE-FG02-99ER45778. This work was also supported in part by the Materials Research Science and Engineering Center (MRSEC) program of NSF award DMR 98-08941 and made use of MRSEC shared facilities supported by NSF under award DMR-9400334. This material is also based on work supported in part under an NSF graduate research fellowship. Special thanks are also given to U. Kolodny and OmniGuide Communications, Inc.

22 January 2002; accepted 13 March 2002

Superplumes from the Core-Mantle Boundary to the Lithosphere: Implications for Heat Flux

Barbara Romanowicz,* Yuancheng Gung

Three-dimensional modeling of upper-mantle anelastic structure reveals that thermal upwellings associated with the two superplumes, imaged by seismic elastic tomography at the base of the mantle, persist through the upper-mantle transition zone and are deflected horizontally beneath the lithosphere. This explains the unique transverse shear wave isotropy in the central Pacific. We infer that the two superplumes may play a major and stable role in supplying heat and horizontal flow to the low-viscosity asthenospheric channel, lubricating plate motions and feeding hot spots. We suggest that more heat may be carried through the core-mantle boundary than is accounted for by hot spot fluxes alone.

Global seismic tomography aims to improve our understanding of mantle dynamics by providing constraints on three-dimensional (3D) temperature and composition with the use of elastic velocities as proxies. Much progress has been made in recent years in resolving increasingly finer details in the 3D distribution of elastic velocities from the inversion of seismic phase and travel time data (*1–3*). In particular, regions of faster-than-average velocity, associated with subduction around the Pacific rim, have revealed a variety of behaviors of lithospheric slabs in the transition zone, some stag-

Seismological Laboratory, University of California, Berkeley, 215 McCone Hall, Berkeley, CA 94720, USA.

*To whom correspondence should be addressed. E-mail: barbara@seismo.berkeley.edu

nant around the 670-km discontinuity, whereas others penetrate into the lower mantle to depths in excess of 1500 km (*4*). These results agree with geodynamic models in which the cold and dense down-going slabs play a driving role in global mantle circulation heated primarily from within (*5*). The detailed morphology and role of upwellings, as manifested by two prominent zones of lower than average velocity in the lowermost mantle and commonly referred to as superplumes, is less clear. Their location, under the south-central Pacific and under Africa, correlates with the global distribution of hot spots, as well as two major geoid highs (*6*). Recent tomographic S wave velocity models suggest that the superplumes rise high above the core-mantle boundary (CMB) (*3*, *7*), and joint seismic-geodynamic studies imply that they may be active upwellings (*8*). However, finer scale resolution is still lacking. In particular, velocity tomography in the transition zone correlates well with slabs but not so well with hot spot distribution or the residual geoid, except at degree 6 (*9*). This could be due to a combination of factors as follows: (i) elastic velocities are sensitive to composition as well as temperature, (ii) the effect of temperature on velocities decreases with increasing pressure (*10*), (iii) wavefront healing effects make it difficult to accurately image low velocity bodies (*11*), and (iv) hot spots may have a shallow origin, independent of the lower mantle superplumes (*12*).

To obtain additional constraints on hotter-than-average features, we turn to the amplitudes of seismic waves, which are sensitive to 3D anelastic structure. Owing to the exponential dependence on temperature of attenuation (*13*), which we shall express in terms of Q^{-1}, where Q is the quality factor, we expect anelastic tomography to highlight hotter than average regions better than standard elastic tomographic approaches.

There have been few attempts at mapping mantle 3D attenuation structure. Travel time and phase observations, in general, can be interpreted in the framework of linear ray theory. Unlike these observations, amplitudes are affected not only by anelastic structure but also by the nonlinear effects of wave propagation through the 3D elastic medium, which causes focusing and scattering of energy (*14*). Because the lateral gradients of elastic structure are not sufficiently well constrained to allow the accurate removal of elastic effects, the resulting contamination of amplitude data can be severe. Particular care must therefore be taken in data selection and methodology in order to extract the intrinsic attenuation signal. Previous studies of lateral variations of Q^{-1} in the upper mantle have noted high-attenuation regions associated with ridges (*15*, *16*) and back arcs (*15*, *17*) and have suggested the existence of a degree 2 in attenuation (*15*, *18*). However, on the global scale, 3D mantle Q^{-1} models have remained largely qualitative.

We developed a waveform tomographic inversion method, originally aimed at constructing global 3D elastic models of the whole mantle (*3*, *19*), that now has been extended to iteratively solve for elastic and anelastic structure in the upper mantle with the use of three-component waveform data of fundamental and higher mode surface waves (*20*). Though the method does not directly account for elastic effects in the amplitudes, which limits the lateral resolution of our Q^{-1} models to $lmax = 8$ (*21*), where $lmax$ is the maximum degree in a horizontal spherical harmonics parametrization, strict data selection criteria are designed to reject data most strongly contaminated by focusing (*22*).

In the top 250 km of the mantle, correlation of high Q regions with shields is seen systematically in North and South America, Eurasia, Australia, and Antarctica, whereas mid-ocean ridges in the Pacific, Atlantic, and Indian Ocean exhibit generally low Q values, as do western Pacific back-arc regions (Fig. 1). This is similar to what is observed in elastic velocity models (*1*–*3*), with regions of high velocity correlated with regions of high Q. A notable exception is an elongated zone of high attenuation in the central Pacific, extending from south of the equator to Hawaii, not seen in *SH* velocity models (*3*, *19*) at these depths. Below 250 km, this tectonics-related Q distribution is gradually replaced by a simpler pattern with two strong

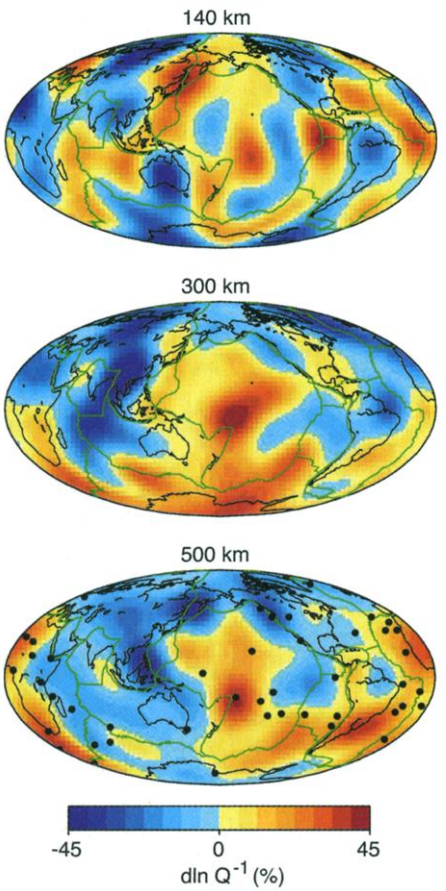

Fig. 1. Maps of lateral variations in Q^{-1} at representative depths in the upper mantle, obtained by joint inversion of three-component waveform data (model *QRLW8*). Black dots are hot spots (*9*), and the global plate boundary system is in green, emphasizing the changing Q^{-1} pattern as depth increases. The two high-attenuation peaks in the transition zone appear to be connected through South America, following the trail of southern hot spots. Temperature contrasts at the center of the high-attenuation regions in the transition zone could be several hundred degrees; however, amplitudes of lateral variations in Q^{-1} are not well constrained.

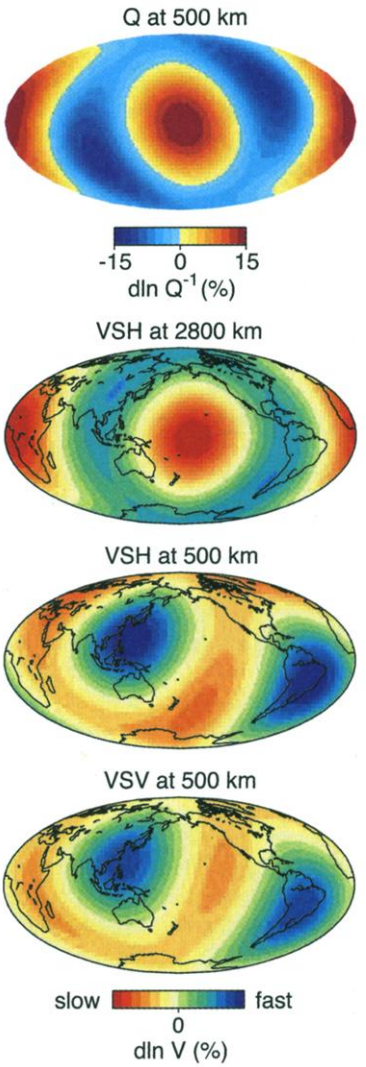

Fig. 2. Comparison of the degree 2 distribution in Q^{-1} in the upper mantle transition zone (depth of 500 km) for model *QRLW8*, with the corresponding distribution in *SH* and *SV* velocity as well as with *SH* velocity at 2800 km. The *SH* model is *SAW24B16* (*3*). The *SV* model, *SAW16BV*, was derived in the course of the present study [Y. Gung, B. Romanowicz, in preparation]. There is no corresponding *SV* velocity model in the deepest mantle, because the sampling in *SV* at those depths is poorer than for *SH*. The velocity models in the transition zone correlate better with slabs than with superplumes.

attenuation maxima centered in the southern Pacific and under Africa throughout the upper mantle transition-zone. At depths greater than 400 km, a majority of hot spots are located above regions of high attenuation.

In model *QRLW8*, the high-attenuation regions in the transition zone coincide in location with the minima in elastic velocity associated with the two superplumes in the lowermost mantle. Correlation between Q in the transition zone and velocity in the last 500 km of the mantle is particularly strong at degree 2 (Fig. 2) but persists at shorter wavelengths. Cross sections in the Pacific (Fig. 3A) and under Africa (Fig. 3B), comparing upper mantle Q^{-1} with lower mantle velocity distributions, emphasize the vertical correspondence of the transition zone low Q zones with the lowermost mantle. The latter "rise" vertically through the lower mantle and have complex shapes, especially under Africa. Because our Q^{-1} model does not extend to the lower mantle and the low-velocity zones are only expressed faintly in the upper half of the lower mantle, where they appear to be narrower and have a complex shape just below the 670-km discontinuity, it is not possible to determine whether the superplumes are simply continuous across this major discontinuity or whether they induce upwellings in the upper mantle through thermal coupling processes. However, our results show that the superplumes must carry enough energy across the lower mantle to create coherent upwelling flow in the upper mantle transition zone, in agreement with some recent mantle flow models (*8*). In contrast, ridges are shallow high-attenuation features, mostly confined to the upper 200 km of the mantle.

The low Q zones in the transition zone connect with shallower ones whose positions are shifted horizontally, suggesting that the upwelling plume-related flow is deflected horizontally below the cold lithosphere toward the Indian and Atlantic mid-ocean ridges under Africa and in the Pacific toward the East Pacific rise and the center of the Pacific plate. In the latter case, the flow is impeded on the west side by the presence of the Fiji-Tonga subduction zone. This deflection occurs at greater depths under the thicker continental lithosphere (~350 km, Fig. 3B) than under the oceanic one (~200 km, Fig. 3A).

This change in direction of the upwelling flow is supported by the presence of significant anisotropy (transverse isotropy), as seen by comparing $V_{SH} - V_{SV}$ cross sections with those of Q^{-1} (Fig. 3, A and B). The existence of horizontal flow related to the spreading of upwelling flow beneath the lithosphere provides a simple explanation for the existence of strong transverse isotropy in the central Pacific, in particular under Hawaii, with *SH* velocity greater than *SV* velocity (*23*). Also, azimuthal anisotropy (not shown), which consistently shows fast directions aligned perpendicular to the ridge in the vicinity of the East Pacific Rise, displays a more complex pattern in the central Pacific (*24*). This is consistent with the spreading of upwelling flow associated with the superplumes into the asthenospheric low-viscosity channel (*25*), which perturbs the ridge-perpendicular lithospheric drag flow and creates a complex horizontal flow pattern in the central Pacific. The "hot" anomaly associated with the Hawaiian hot spot, as seen in the Q^{-1} models (Fig. 3A), is primarily expressed at shallow depth (less than 300 km) and appears to be "fed" from the more southerly upwelling by horizontal flow beneath the lithosphere.

These results suggest a potentially important role for superplumes in the dynamics of the mantle: dynamic processes may take place in the shallow mantle, where hot material injected

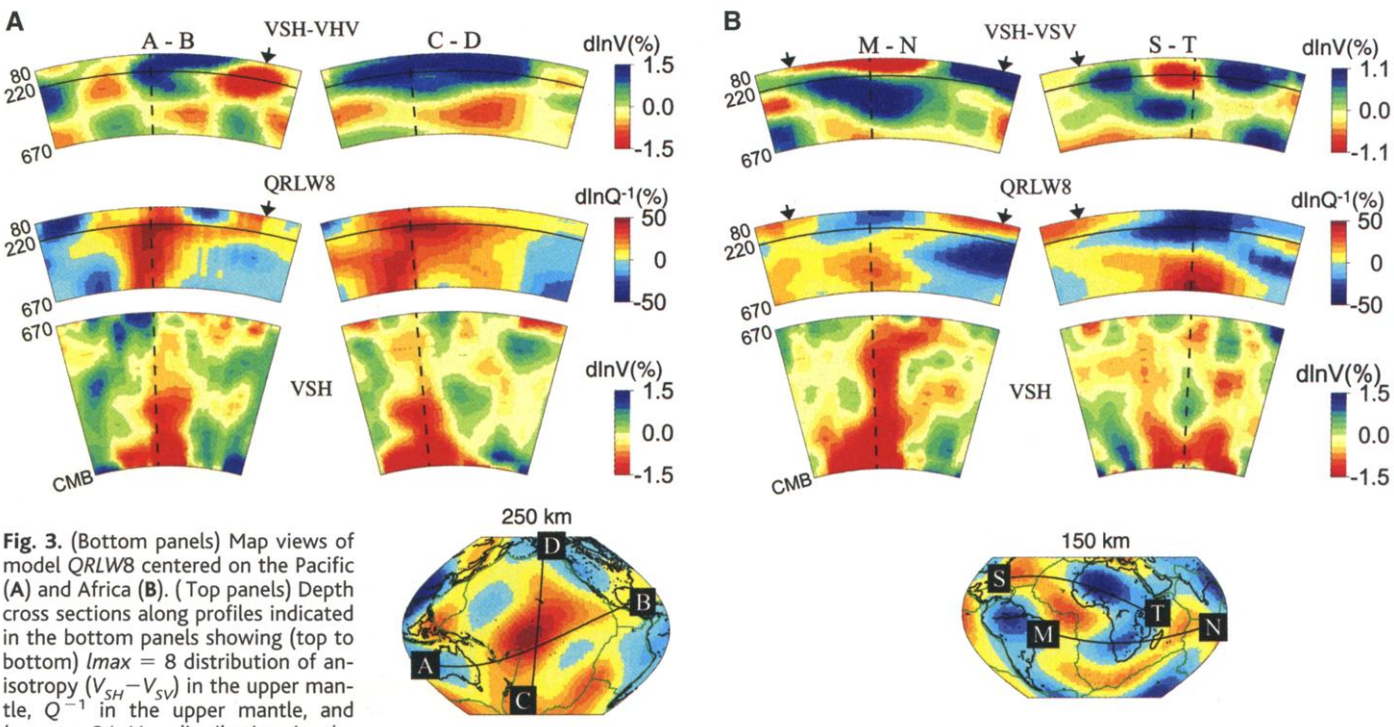

Fig. 3. (Bottom panels) Map views of model *QRLW8* centered on the Pacific (**A**) and Africa (**B**). (Top panels) Depth cross sections along profiles indicated in the bottom panels showing (top to bottom) *lmax* = 8 distribution of anisotropy ($V_{SH}-V_{SV}$) in the upper mantle, Q^{-1} in the upper mantle, and *lmax* = 24 V_{SH} distribution in the lower mantle. The upper mantle cross sections start at 80-km depth because our Q^{-1} modeling does not have resolution above that depth. Mid-ocean ridge positions are indicated by arrows. The high-attenuation regions in the transition zone are positioned above the lowermost mantle low-velocity minima. We show $V_{SH}-V_{SV}$ rather than velocities themselves because the latter are contaminated by anisotropy, which hides the thermal signal. Zones of positive $V_{SH}-V_{SV}$ in the uppermost mantle (blue) correspond to zones where the high Q^{-1} regions are shifted horizontally with respect to their transition zone location. This shift in Q^{-1} is well resolved, as indicated by synthetic tests. The superplumes have complex shapes, especially in Africa, where the upwelling appears to have several branches, consistent with observations of experimental fluid dynamics (*39*). Ridges are generally shallow features (e.g., at S, N, and B), except in the south Atlantic (at M), where the ridge is also connected to the deeper high-attenuation zone under South America. Note the negative $V_{SH}-V_{SV}$ at shallow depth under the African cratons, consistent with other studies (*40*). Maps and cross sections show relative variations with respect to the average velocity or Q^{-1} at each depth, for which the relation to temperature is not well determined, nor is the amplitude of the lateral variations in Q^{-1} well constrained. Therefore, it is not possible to directly compare temperatures beneath ridges and in the transition zone low Q regions.

by the superplumes lowers the viscosity of the asthenosphere (*8*, *26*), lubricating the motion of the lithospheric plates. In particular, this would allow for efficient slab pull in the Pacific and contribute to heating of the continental lithosphere under Africa (*6*, *27*). Most hot spots are derived from the two main upwellings. Exceptions may be hot spots in North America and perhaps Iceland, whose signature in the Q^{-1} models is lost below 400 km and whose deep or shallow origin has been the subject of vigorous debate (*7*, *28*, *29*). Because material from the large upwellings progressively mixes with the asthenosphere, the relation of the position of different hot spots with respect to the centers of the large upwellings may provide clues to their distinctive geochemical signatures (*30*), particularly in view of the noted correlation of the lower mantle superplumes with the Dupal anomaly (*31*).

Previous suggestions on the relation of major flood basalts to the two superplumes (*32*) and the stability of absolute hot spot locations (*33*) combined with the results of the present study indicate that the two large lower mantle upwellings may not be small instabilities in the present mantle convective system. In particular, the estimate of ~10% heat from the core carried by plumes (*34*) may need to be revised to account not only for hot spot flux but also for heat carried horizontally in the asthenosphere and eventually contributed to the ridge system.

References and Notes

1. G. Masters, S. Johnson, G. Laske, B. Bolton, *Philos. Trans. R. Soc. London Ser. A* **354**, 1385 (1996).
2. Y. J. Gu, A. M. Dziewonski, W.-J. Su, G. Ekström, *J. Geophys. Res.* **106**, 11169 (2001).
3. C. Mégnin, B. Romanowicz, *Geophys. J. Int.* **143**, 709 (2000).
4. Y. Fukao, S. Widiyantoro, M. Obayashi, *Rev. Geophys.* **39**, 291 (2001).
5. D. Bercovici, Y. Ricard, M. A. Richards, *Geophys. Monogr. Am. Geophys. Union 121* (American Geophysical Union, Washington, DC, 2000), p. 5.
6. B. Hager, R. W. Clayton, M. A. Richards, R. P. Comer, A. M. Dziewonski, *Nature* **313**, 541 (1985).
7. J. Ritsema, H. van Heijst, J. Woodhouse, *Science* **286**, 1925 (1999).
8. A. M. Forte, J. X. Mitrovica, *Nature* **410**, 1049 (2001).
9. M. Richards, B. H. Hager, N. H. Sleep, *J. Geophys. Res.* **93**, 7690 (1988).
10. S. I. Karato, *Geophys. Res. Lett.* **20**, 1623 (1993).
11. G. Nolet, F. A. Dahlen, *J. Geophys. Res.* **105**, 19043 (2000).
12. D. L. Anderson, *Science* **293**, 2016 (2001).
13. J. B. Minster, D. L. Anderson, *Philos. Trans. R. Soc. London Ser. A* **299**, 319 (1981).
14. For example, high-frequency body waves traveling through slabs arrive early but are defocused.
15. B. Romanowicz, *J. Geophys. Res.* **100**, 12375 (1995).
16. F. J. L. Reid, J. H. Woodhouse, H. H. van Heist, *Geophys. J. Int.* **145**, 695 (2001).
17. E. G. Roth, D. Wiens, L. M. Dorman, J. Hildebrand, S. Webb, *J. Geophys. Res.* **104**, 4795 (1999).
18. N. Suda, N. Shibata, Y, Fukao, *Geophys. Res. Lett.* **18**, 1119 (1991).
19. X. D. Li, B. Romanowicz, *J. Geophys. Res.* **101**, 22245 (1996).
20. The inversion involves comparison of observed waveforms of surface waves and body waves, with synthetics computed using normal mode theory. It proceeds in two steps. In the first step, waveform phases are aligned by constructing 3D elastic models of the mantle separately for *SH* (transverse component) and *SV* (vertical and longitudinal component) using the coupled-mode approach developed for *SH* models (*19*). In the second step, we invert for Q^{-1}, using three-component data and starting from a spherically symmetric reference Q^{-1} model (*35*), as well as the 3D velocity models obtained in the previous step. An additional variance reduction of ~7% is thus obtained. For this specific study, which is focused on the retrieval of Q^{-1} structure, velocity models are parametrized up to maximum spherical harmonics degree *smax* = 16 horizontally with the use of 16 B-splines vertically (throughout the mantle). The Q^{-1} models that have *smax* = 8 in the horizontal direction and 7 B-splines in the vertical direction use only fundamental and higher mode surface wave packets and are therefore restricted to the upper mantle. For crustal corrections, we use model Crust 5.1 (*36*) for velocities. We invert only for Q^{-1} structure below 80 km, correcting for shallow structure using information on Moho variations from Crust 5.1. Frequency dependence of Q^{-1} is not resolvable in the period range considered. Lateral variations in the lower mantle where Q^{-1} is low may be hard to detect.
21. N. D. Selby, J. H. Woodhouse, *Geophys. J. Int.* **142**, 933 (2000).
22. Our confidence in the stability of the Q^{-1} patterns derives from the comparison of models obtained independently using Z, L, or T component data, as well as bootstrapping and resolution experiments. The resolution experiments confirm our ability to distinguish structures in the uppermost 250 km from those at larger depth, whereas inversions using different components confirm that contamination by elastic effects does not dominate the observed patterns. [Y. Gung, B. Romanowicz, in preparation].
23. G. Ekström, A. M. Dziewonski, *Nature* **394**, 168 (1997).
24. J. P. Montagner, T. Tanimoto, *J. Geophys. Res.* **96**, 20337 (1991).
25. C. Gaboret, A. M. Forte, J. P. Montagner, *EOS* **82**, 47 (2001).
26. The existence of a low-viscosity channel under the lithosphere has been recognized for some time from modeling of glacial rebound as well as joint modeling of gravity and seismological data (*37*, *38*).
27. A. Nyblade, S. Robinson, *Geophys. Res. Lett.* **21**, 765 (1994).
28. C. Wolfe, I. T. Bjarnason, J. VanDecar, S. C. Solomon, *Nature* **385**, 245 (1997).
29. G. Foulger, D. G. Pearson, *Geophys. J.* **145**, F1 (2001).
30. S. R. Hart,, E. H. Hauri, L. A. Oschmann, J. A. Whitehead, *Science* **256**, 517 (1995).
31. P. Castillo, *Nature* **336**, 667 (1988).
32. K. Burke, *Eos* **82**, F1134 (2001).
33. W. J. Morgan, *Nature* **230**, 42 (1971).
34. N. Sleep, *J. Geophys. Res.* **95**, 6715 (1990).
35. J. J. Durek, G. Ekström, *Bull. Seismol. Soc. Am.* **86**, 144 (1996).
36. W. D. Mooney, G. Masters, G. Laske, *J. Geophys. Res.* **103**, 727 (1998).
37. G. Davies, M. Richards *J. Geol.* **100**, 151 (1992).
38. J. X. Mitrovica, A. M. Forte *J. Geophys. Res.* **102**, 2751 (1997).
39. A. Davaille, *Nature*, **402**, 756 (1999).
40. V. Babuška, J.-P. Montagner, J. Plomerova, N. Girardin, *Pure Appl. Geophys.* **151**, 257 (1998).

41. We thank A. Forte and a second reviewer for constructive comments, and A. Davaille for helpful discussions. Supported by NSF (grant no. EAR-0001965). It is BSL contribution no. 0205.

27 December 2001; accepted 8 March 2002

Evidence for an Ancient Osmium Isotopic Reservoir in Earth

Anders Meibom[1]* and Robert Frei[2]

Iridosmine grains from placer deposits associated with peridotite-bearing ophiolites in the Klamath mountains have extremely radiogenic $^{186}Os/^{188}Os$ ratios and old Re-Os minimum ages, from 256 to 2644 million years. This indicates the existence of an ancient platinum group element reservoir with a supra-chondritic Pt/Os ratio. Such a ratio may be produced in the outer core as a result of inner core crystallization that fractionates Os from Pt. However, if the iridosmine Os isotopic compositions are a signature of the outer core, then the inner core must have formed very early, within several hundred million years after the accretion of Earth.

Osmium has two radiogenic isotopes, ^{186}Os and ^{187}Os. ^{190}Pt decays to ^{186}Os with a half-life of ~449.4 billion years (Gy) (*1*), and ^{187}Re decays to ^{187}Os with a half-life of ~41.6 Gy (*2*, *3*). Therefore, the Os isotopic system may be used to track ancient fractionated highly siderophile element (HSE) reservoirs. For example, it has been argued that coupled enrichments in ^{186}Os and ^{187}Os in the deep-rooted Hawaiian and Noril'sk plume-derived lavas (*4*–*8*) are a signature of the outer core. In this model, radiogenic Os isotopic compositions have developed as a result of early fractionation of Os from Re and Pt during crystallization of the inner core that caused high Pt/Os and Re/Os elemental ratios to build up in the outer core. Because the lower mantle is expected to have low concentrations [~1 part per billion (ppb)] and the core high concentrations (>100 ppb) of HSEs (including Os, Re, and Pt), it would only require small amounts of outer core material to enter the lower mantle in order to imprint an outer core Os isotopic signature on plumes ascending from the core-mantle boundary (*4*–*9*).

[1]Geological and Environmental Sciences, 320 Lomita Mall, Stanford University, CA 94305-2115, USA. [2]Geological Institute, University of Copenhagen, Øster Voldgade 10, DK-1350 Copenhagen, Denmark.

*To whom correspondence should be addressed. E-mail: meibom@pangea.stanford.edu